Anomalous sound propagation and slow kinetics in dynamically compressed amorphous carbon

Evan J. Reed,* Amitesh Maiti, and Laurence E. Fried
Physical and Life Sciences Directorate, Lawrence Livermore National Laboratory, Livermore, California 94550, USA
(Received 23 June 2009; published 19 January 2010)

We have performed molecular-dynamics simulations of dynamic compression waves propagating through amorphous carbon using the Tersoff potential and find that a variety of dynamic compression features appear for two different initial densities. These features include steady elastic shocks, steady chemically reactive shocks, unsteady elastic waves, and unsteady chemically reactive waves. We show how these features can be distinguished by analyzing time-dependent propagation speeds, time-dependent sound speeds, and comparison to multiscale shock technique (MSST) simulations. Understanding such features is a key challenge in quasi-isentropic experiments involving phase transformations. In addition to direct simulations of dynamic compression, we employ the MSST and find agreement with the direct method for this system for the shocks observed. We show how the MSST can be extended to include explicit material viscosity and demonstrate on an amorphous Lennard-Jones system.

DOI: 10.1103/PhysRevE.81.016607 PACS number(s): 43.35.+d, 62.50.Ef

I. INTRODUCTION

The generation of high-pressure compression waves in materials is a primary tool for measuring high-pressure properties. Material pressures achieved under dynamic compression are much higher than those possible to achieve under static compression, more than 10 s of Mbars versus a few Mbar for the latter. Dynamic compression waves can be lumped into one of two categories: (1) shock waves and (2) quasi-isentropic waves. Steady shock waves compress the material to thermodynamic states on the shock Hugoniot. Quasi-isentropic waves, also referred to as ramp compression waves, take the material to thermodynamic states that lie between the material isentrope and the shock Hugoniot. Distinguishing between these types is required to understand and interpret the thermodynamic states being produced in the material. However, challenges present themselves when attempting to make this distinction, particularly on the nanosecond to picosecond time scales of molecular-dynamics (MD) simulations and emerging laser-based and other experimental capabilities [1–3]. Time-dependent chemical processes, phase transformations, and anomalous properties of the material equation of state can lead to compression wave propagation that exhibits characteristics of both shock and ramp waves. Considerable attention has been given to interpreting experiments performed in such regimes (see, e.g., Refs. [4–6])

Steady shock waves compress the material to thermodynamic states on the shock Hugoniot and propagate at a constant speed. Shock waves have the property that they are time independent in a reference frame moving at the shock speed, i.e., the density $\rho(x,t)$ has the form $\rho(x-v_s t)$ where v_s is the propagation speed. Unsteady shocks are similar to shock waves but propagate at a speed that is not constant and the thermodynamic states produced therefore deviate from the shock Hugoniot states to some extent. Unlike shocks, ramp waves take the material to thermodynamic states that lie between the material isentrope and the shock Hugoniot. Such waves are presumably isentropic in the limit where the strain rate becomes vanishing, but the strain rates achieved in experiments can range in excess of 10^{10} s^{-1} resulting in potentially significant deviations from an isentrope. Unlike shocks, there are no moving reference frames in which ramp waves are time independent, i.e., different parts of the wave can propagate at different speeds.

Whether a compression wave is a shock or ramp is ordinarily determined largely by the time dependence of the pressure supplied by the drive on the sample. While most materials support shock waves, some do not within certain pressure regimes where only ramp waves are exhibited. The latter type of ramp waves are intrinsic to the material, independent of the pressure drive time dependence, and are the type that we will discuss in this work.

Molecular-dynamics simulations have proven to be an effective tool to simulate shocked materials, but little attention has been given to dealing with materials that exhibit more complicated behaviors like intrinsic ramp waves and unsteady waves with slow kinetic processes. In this work, we perform molecular-dynamics simulations of dynamic compression in amorphous carbon, a material that exhibits both shock waves and ramp waves. For two different initial densities, we find that a wave with fast rise time (under 1 ps) launched into this material decomposes into a complicated wave structure including sharp and diffuse shock waves and ramp waves. Using a combination of molecular-dynamics techniques including direct methods and the multiscale shock technique (MSST), we show that the origin of the wave structure can be understood and predicted.

In thermodynamic regimes away from phase boundaries, materials ordinarily exhibit an increase in sound speed with increasing pressure. When a high-pressure compression wave is launched into the material, the sound speed dependence on pressure will cause it to steepen to form a shock as it propagates. High pressure portions of the wave propagate more quickly than lower pressures resulting in an overtake of the lower pressure wave front. Amorphous materials have been shown to exhibit significant pressure regimes in which the sound speeds decrease with increasing pressure. Such

*reed23@llnl.gov

regimes lead to anomalous behavior when a high-pressure amplitude wave is launched into the material. In this case, high-pressure portions of the wave propagate more slowly than lower pressure portions, resulting in a wave that spreads out with time rather than steepening into a shock. In fact, a shock wave with a fast rise time launched into such a material will spread out with time as it propagates. Some amorphous materials have been utilized with gas-gun fired projectile experiments to generate pressure waves with strain rates much slower than shock waves to compress materials more nearly along an isentrope than the shock Hugoniot [7].

Amorphous materials also have the property that the Hugoniot elastic limit can potentially be zero, as in a liquid. However, the kinetics of plastic deformation processes are slow when the pressure and temperature are low. Early theoretical work showed that such behavior can lead to the formation of a pressure wave that obeys the Hugoniot relations but has no sharp, shocklike features [8]. The formation of such a wave may be difficult to distinguish from the diffuse ramp waves generated via the anomalous sound speed mechanism, although the underlying origin is fundamentally different.

Shock waves have been studied in a wide rage of carbon allotropes with varying degrees of order. Dynamic compression experimental investigations on carbon include vitreous carbon [9], diamond [10,11], and graphite [12]. A number of atomistic simulations of dynamic compression of various forms of carbon have also been performed including diamond [13–15] and graphite [16]. Atomistic dynamic compression simulations of amorphous forms of carbon have not been reported, but single shocks in silica glasses have been studied [17–19].

In this work, we perform molecular-dynamics simulations of shocked amorphous carbon to explore the range of dynamic compression features that appear. We utilize the interatomic potential due to Tersoff [20] which has been developed for simulation of amorphous phases of carbon. We consider two different initial material densities and find qualitatively different behavior of the wave upon dynamic compression. In addition to direct simulations of dynamic compression, we employ the MSST [21,22] which has been utilized to study phase transformations and chemical reactions in shocked materials [16,23–25]. Good agreement with the direct method for this system is observed for the shocks, both in the thermodynamic states visited by the shock and the time dependence of the waves. While the MSST is designed to simulate only steady shock waves, we find that it is an effective tool in predicting the existence of unsteady ramp waves due to anomalous sound speed properties. The latter is a unique consequence of the Rayleigh-based constraint employed by MSST.

II. MSST COMPUTATIONAL SCHEME

The MSST combines atomistic simulations with the Navier-Stokes equations for compressible flow. It has been demonstrated to accurately reproduce the sequence of thermodynamic states throughout the reaction zone of detonating explosives with analytical equations of state [26]. Instead of simulating a shock wave within a large computational cell with many atoms (the direct approach), the computational cell of the multiscale technique follows a Lagrangian point through the shock wave, enabling simulation of the shock wave with significantly fewer atoms and significantly lower computational cost. Linear scaling of computational work with simulation duration has enabled durations of hundreds of picoseconds with tight-binding molecular dynamics, representing a computational speedup of 10^9 over the direct shock-simulation approach [23,25]. It has also made possible density-functional theory based shock studies [16,24]. The multiscale shock technique simulates steady shock waves (that is, constant shock speed) by time-evolving equations of motion for the atoms and volume of the computational cell to constrain the shock-propagation-direction stress to the Rayleigh line and energy to the Hugoniot energy condition. For a specified shock speed, the latter two relations describe a steady planar shock wave within continuum theory.

The MSST computational scheme utilized in part of this work is closely related to our previously reported scheme based on the Euler equations for compressible flow [21,22]. Here we review the technique and show how the scheme can be extended to the Navier-Stokes equations without thermal diffusion by including an explicit viscous component of the pressure.

The Navier-Stokes equations represent the conservation of mass, momentum, and energy, respectively, everywhere in the wave,

$$\frac{d\rho}{dt} + \rho\frac{\partial u}{\partial x} = 0, \tag{1}$$

$$\frac{du}{dt} + \tilde{v}\frac{\partial}{\partial x}\left(p - \mu\frac{\partial u}{\partial x}\right) = 0, \tag{2}$$

$$\frac{d\tilde{e}}{dt} + \left(p - \mu\frac{\partial u}{\partial x}\right)\frac{d\tilde{v}}{dt} = 0, \tag{3}$$

and complete time derivatives are $\frac{d}{dt} \equiv \frac{\partial}{\partial t} + u\frac{\partial}{\partial x}$. We seek solutions of the Navier-Stokes equations that are steady in the frame of the shock wave moving at speed v_s by making the substitution $x \rightarrow x_0 + v_s t$. This substitution, and integration yields a variation in the Hugoniot relations,

$$u - u_0 = (v_s - u_0)\left(1 - \frac{\rho_0}{\rho}\right), \tag{4}$$

$$p - \frac{\mu}{\tilde{v}}\dot{\tilde{v}} - p_0 = (u_0 - v_s)^2\rho_0\left(1 - \frac{\rho_0}{\rho}\right), \tag{5}$$

$$\tilde{e} - \tilde{e}_0 = p_0\left(\frac{1}{\rho_0} - \frac{1}{\rho}\right) + \frac{(u_0 - v_s)^2}{2}\left(1 - \frac{\rho_0}{\rho}\right)^2. \tag{6}$$

Here, ρ is the density, u is the local (laboratory) material velocity, $\tilde{v} = 1/\rho$ is the specific volume, p is the uniaxial stress ($p = -\sigma_{xx}$), $\tilde{e}$ is the energy per unit mass, and μ is a viscosity parameter. Variables with subscripts 0 are the values before the shock wave and we take $u_0 = 0$; i.e., the material is initially at rest in the laboratory frame. The Navier-

Stokes viscous pressure, $-\mu' \frac{\partial u}{\partial x}$, has been evaluated in the moving reference frame of the material where $\frac{\partial}{\partial x} = -\frac{1}{v_s - u}\frac{\partial}{\partial t}$. These equations are obeyed by a material element flowing at speed u through a steady shock wave.

We seek molecular-dynamics equations of motion for the atoms and volume of the computational cell that obey these constraints; these are,

$$Q\ddot{\tilde{v}} = \sum_i m_i A\dot{\vec{s}}_i \cdot \frac{dA}{dv}\dot{\vec{s}}_i - \frac{d\phi}{dv} - \frac{v_s^2}{\tilde{v}_0^2}(\tilde{v}_0 - \tilde{v}) - p_0 - \mu\frac{\dot{\tilde{v}}}{\tilde{v}}, \quad (7)$$

$$\ddot{\vec{s}}_i = \frac{-1}{m_i}A^{-1}\frac{\partial\phi}{\partial\vec{r}_i} - G^{-1}\dot{G}\dot{\vec{s}}_i + M\frac{\mu\dot{\tilde{v}}^2}{m_i\tilde{v}}\frac{\dot{\vec{s}}_i}{\sum_j |A\dot{\vec{s}}_j|^2}. \quad (8)$$

Here, Q is a masslike parameter for the volume, $M = \Sigma_i m_i$, $G \equiv A^T A$, $\phi(\{\vec{r}_i\})$ is the potential energy of the system, v is the computational cell volume, and we utilize the scaled coordinate scheme of Ref. [27] where $\vec{r} \equiv A\vec{s}$ and $\dot{\vec{r}}_i \equiv A\dot{\vec{s}}_i$ where A contains the computational cell lattice vectors in columns and $\vec{s}_i$ is the scaled position of atom i. Uniaxial strain of the computational cell is utilized since the shock is planar and $\frac{dA}{dv}$ is a matrix corresponding to the direction of the uniaxial strain; i.e., A is only allowed to change with one degree of freedom. These equations have the conserved quantity, $\tilde{e}_0 = \tilde{e} + \frac{1}{2}Q\dot{\tilde{v}}^2 - \frac{v_s^2}{2}(1 - \frac{\tilde{v}}{\tilde{v}_0})^2 - p_0(\tilde{v}_0 - \tilde{v})$ with $\tilde{e} = \Sigma_i \frac{1}{2M} m_i |A\dot{\vec{s}}_i|^2 + \frac{1}{M}\phi(\{\vec{r}_i\})$. We have shown this is equivalent to Eq. (6) when equipartition is achieved. Time averaging of Eq. (7) reproduces the Rayleigh condition [Eq. (5)] [22]. Therefore these equations of motion satisfy the thermodynamic conditions of a material element flowing through a steady shock. We have experimented with adding to the right side of Eq. (8), $\beta M\dot{\vec{s}}_i(\tilde{e} - \tilde{e}_0 + \frac{1}{2}Q\dot{\tilde{v}}^2 - p_0(\tilde{v}_0 - \tilde{v}) - \frac{v_s^2}{2}(1 - \frac{\tilde{v}}{\tilde{v}_0})^2)/\Sigma_i \frac{1}{2} m_i |A\dot{\vec{s}}_i|^2$. This term is zero if the numerical integration is error free. Setting β to be nonzero aids energy conservation for long MD runs and potentially enables the use of longer integration time steps.

Equations (7) and (8) are the equations of motion derived from the Hamiltonian based on the conserved quantity with the exception of the last term in each equation which represents a non-Hamiltonian viscous term. This term acts as an explicit damping term in the volume equation of motion. Energy removed through volume damping is irreversibly supplied to the atoms through the last term of Eq. (8). We note that even when $\mu = 0$ (corresponding to the case in Ref. [21]) the volume equation of motion is damped by an intrinsic coupling of the volume to the motion of the atoms via scaled coordinates. The level of intrinsic viscosity provided by scaled coordinates may not necessarily be representative of the shock when spatial gradients are large (near the shock front) since the multiscale approach assumes that spatial gradients in density and other quantities are small compared with the inverse correlation length in the material. Setting $\mu \neq 0$ introduces *extra* viscosity which we will show can potentially be used to achieve better agreement with direct simulations of shock wave profiles near the shock front.

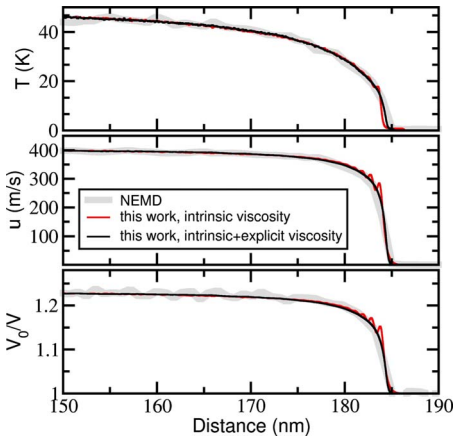

FIG. 1. (Color online) Amorphous Lennard-Jones shock wave profiles computed using the NEMD approach and the multiscale approach (this work) with and without extra (explicit) viscosity. Good agreement is achieved due to the Rayleigh constraint employed by MSST. Utilization of some explicit viscosity brings the multiscale simulations into better agreement with NEMD at short distances behind the shock front.

Application to amorphous Lennard-Jones

Amorphous materials possess many microscopic metastable states along the shock reaction or transition pathway. To validate the multiscale technique performance on a simple example of such a material, we consider the amorphous state of a material with atoms interacting through the Lennard-Jones potential. The material exhibits a series of metastable states during plastic deformation.

Figure 1 shows a comparison of shock profiles between the direct method (also often referred to as nonequilibrium molecular dynamics, or NEMD) and the multiscale technique. We utilized the Lennard-Jones potential with parameters approximately representative of Argon ($\sigma = 3.405$ Å and $\varepsilon/k_B = 119.8$ K) and generated amorphous computational cells by rapidly quenching from a liquid to $T \approx 1$ K. The potential energy of the utilized amorphous phase is 90% of the potential energy of the fcc crystal of the same density; $p_0 = 0.13$ GPa. Multiscale simulations employed 23 400 atoms. NEMD simulations utilized around 1 million atoms and a piston speed of 400 m/s which generated a shock propagating at 2.15 km/s. The shock was allowed to propagate 185 nm to approach a steady wave profile. Figure 1 shows that the temperature, particle speed u, and density of the NEMD profile are all in good agreement with profiles calculated using the multiscale technique.

The multiscale curve with intrinsic viscosity only ($\mu = 0$) exhibits some oscillatory behavior at the beginning of the simulation followed by a smooth adherence to the NEMD curve. We utilized a parameter $Q = 10^{-13}$ kg^2/m^4 and we find that similar behavior is exhibited over a range of Q (from about 4×10^{-14} to 4×10^{-13} kg^2/m^4). Some oscillatory behavior in NEMD simulation is averaged out due to the 1 nm bin size used for averaging. The lack of significant oscillatory behavior in the NEMD curve suggests that the amount of viscosity intrinsically present in the multiscale simulation is less than experienced by the shock in the NEMD simula-

tion. We speculate that this is due to the presence of large spatial gradients at the shock front in the NEMD simulation which can facilitate the excitation of vibrational modes or plastic deformation. Such large spatial gradients are not present in the multiscale simulation.

Figure 1 also shows a multiscale curve computed using some explicit viscosity (with $\mu=1.5\times10^{-4}$ kg/m/s). This viscosity acts in addition to the intrinsic viscosity already present and smoothes out the volume oscillations to achieve good agreement with NEMD even at short distances behind the shock front. Taking the limit $Q\rightarrow0$ reduces Eq. (7) to first order when $\mu\neq0$. The $\mu\neq0$ curve in Fig. 1 is in this limit where Q no longer plays a significant role and the volume behaves in an overdamped fashion. Regardless of whether explicit viscosity is utilized, agreement with the NEMD curve improves with distance behind the shock front where spatial gradients of thermodynamic quantities in the NEMD simulation become less significant. In this regime, the simulation trajectory is largely independent of the empirical parameters (μ and/or Q) that serve to constrain the system since the response time scale of the thermostat is much faster than changes in thermodynamic state due to phase transformations within the computational cell.

A number of accelerated molecular-dynamics methods have been developed for calculating the properties of shocked materials. Like MSST, some of these methods utilize thermodynamic constraints on a computational cell that is usually smaller than a NEMD computational cell. These techniques utilize a constant volume constraint [28,29], constant stress constraint [30], and a combination of NEMD and constant volume constraint [31]. The MSST is distinguished from these methods by its aim to enable simulation of the material between the initial and final states; i.e., it takes the material though the same thermodynamic trajectory as an NEMD simulation of a shock when compression is slow enough for stress to be a well-defined quantity. This is demonstrated by Fig. 1 and other figures in this work. Previous work shows that this property is a result of the Rayleigh line constraint, unique to the MSST [26]. The physically correct pathway described by the Rayleigh constraint also gives rise to sonic stability conditions that prevent simulation of waves that are unphysical [21,26]. These stability properties are employed in the next section to distinguish shock waves from other types of dynamic compression waves.

III. AMORPHOUS CARBON

We now consider the generation of dynamic compression waves in amorphous carbon, described by the Tersoff potential [20]. Figure 2 shows the simulation cell for direct compression simulations. In these simulations, a sharp shock is generated next to the yellow piston and allowed to propagate into the computational cell. The shock is generated by moving the piston to the right at a constant speed. The piston is instantaneously accelerated to its constant speed, yielding a fast, subpicosecond rise time for the pressure wave that propagates away. Periodic boundary conditions transverse to the shock-propagation direction mimic an infinite planar wave. The cell has a square periodic cross section of dimensions 3.25×3.25 nm and a length of 1.95 μm, with a total of $\sim2.5\times10^6$ atoms. The piston is a slab of thickness 2 nm consisting of the same amorphous structure with atom positions fixed relative to each other. The initial amorphous structure was generated using the annealing method described by Tersoff [20]. The initial temperature is 300 K. MSST simulations performed in this section utilized a computational cell masslike parameter Q ranging from 3×10^{-11} to 3×10^{-10} kg^2/m^4 with zero explicit viscosity, $\mu=0$.

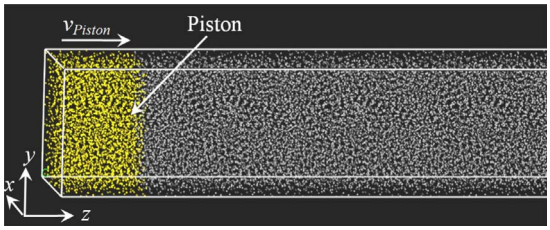

FIG. 2. (Color online) Part of the simulation cell used for NEMD runs in dense a-carbon ($\rho=2.38$ g/cm^3). The cell has a square periodic cross section (parallel to xy plane) of dimensions 3.25 nm$\times$3.25 nm and a length of 1.95 μm (z direction), with a total of $\sim2.5\times10^6$. A slab of thickness 2 nm (atoms in yellow) at one end is defined as the piston, which is moved at a constant speed along the z direction.

Figure 3(a) shows the density states achieved during a series of MSST simulations for a range of shock velocities. For shock speeds below 14.5 km/s, the density of the system does not change; i.e., no shock compression occurs. For shock speeds above 14.5 km/s, the system undergoes shock compression to a higher density. Such a sharp transition in shock density suggests that states intermediate in density cannot be achieved via a single shock wave. Figure 4 shows schematically how such behavior can arise if the material isentrope has the property that $\frac{\partial^2 p_{zz}}{\partial V^2}<0$ around the initial pressure, where p_{zz} is the pressure component in the propagation direction. The path in $p-V$ space that MSST constrains the material to is a straight line. Figure 4 shows how such a constraint can lead to a discontinuity shock in densities at some critical shock speed. Figure 3(a) indicates that shocks with speeds greater than 14.5 km/s will be stable, single shocks and that shocks to low densities are likely to become ramp waves due to the anomalous curvature of the isentrope. The leading edge of the ramp wave will propagate at 14.5 km/s.

Figure 3(b) shows the material density in an NEMD simulation when the piston is given a speed of 6.3 km/s. The resulting wave propagates at a steady speed of 14.8 km/s and appears to be a single, steady shock wave as predicted by MSST. The density of an MSST simulation with shock speed chosen to be 14.8 km/s is overlaid in orange and reveals good agreement with the density and time scale of the NEMD shock.

Figure 3(c) shows the material density in an NEMD simulation when the piston is given a slower speed of 5.0 km/s. The resulting wave consists of a fast rise in density followed by a slower change in density, followed finally by a faster change to the final density. We note that these features result

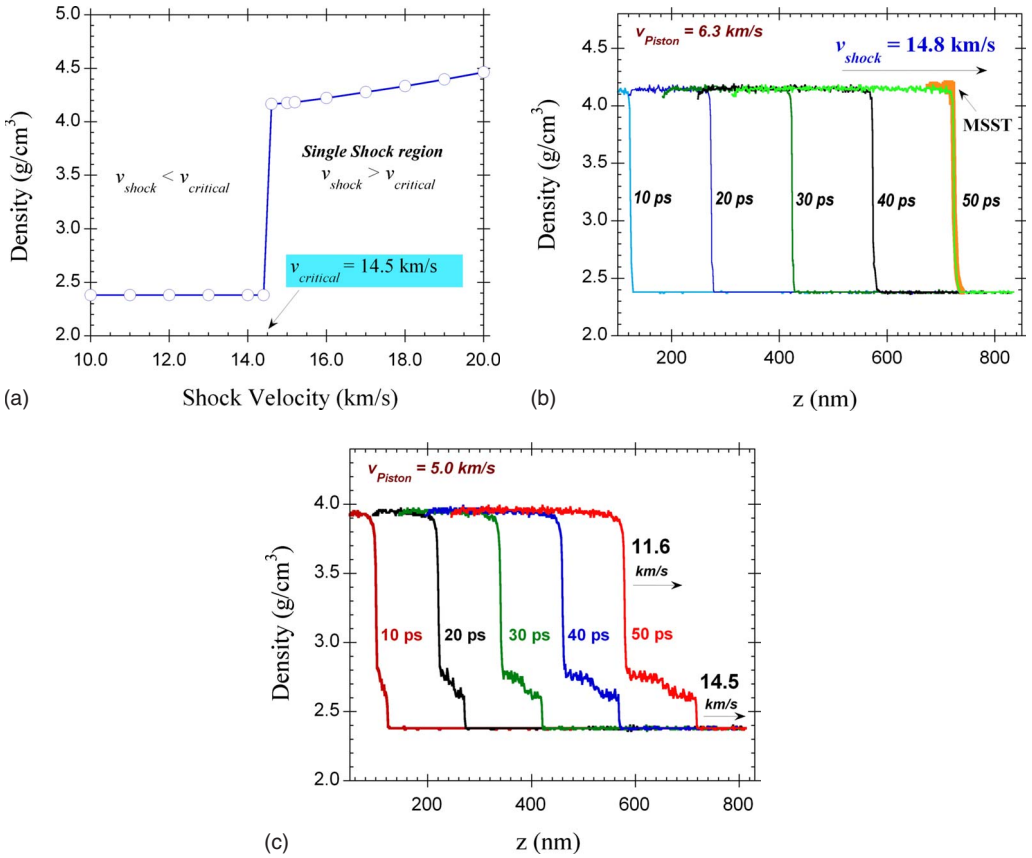

FIG. 3. (Color online) Dynamic compression of dense a-carbon (ρ=2.38 g/cm^3). (a) MSST-computed final density as a function of shock velocity, indicating a sharp transition in the nature of shock propagation at a critical velocity of 14.5 km/s; NEMD-computed wave propagation for: (b) v=14.8 km/s ($v > v_{\text{critical}}$) displaying a single sharp front, and (c) v=11.6 km/s (i.e., $v < v_{\text{critical}}$), showing a more complicated wave structure. In (b), the NEMD-computed shock front agrees well with the MSST-computed shock front (superimposed on the 50 ps front).

from intrinsic properties of the material rather than a time-dependent piston drive. The leading shocklike wave has a speed of 14.5 km/s, the speed predicted by MSST. The high-density portion of the wave propagates at 11.6 km/s and appears to have a steady propagation speed, consistent with a steady shock wave. The length of the intermediate portion grows in time, suggesting a ramp wave or an unsteady shock. These cases cannot be distinguished without further insight, to be discussed later.

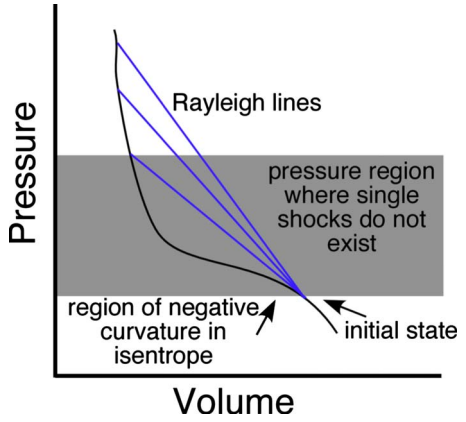

FIG. 4. (Color online) Schematic illustrating how a region of negative curvature in a material isentrope can lead to a region of pressure inaccessible by a single shock. Possible single shocks are depicted by straight Rayleigh lines. The Rayleigh line that is tangent to the isentrope in the initial state defines the lowest possible pressure shock.

For comparison, simulations on a lower initial density amorphous structure were also performed. For this structure (ρ=2.23 g/cm^3), all cell dimensions were increased by 2.2% and the atom positions annealed before performing the NEMD simulation. Figure 5(a) shows the density states achieved during a series of MSST simulations for a range of shock velocities. The results of these simulations are qualitatively similar to those of Fig. 3(a) except the shock speed of the discontinuity is now around 12.5 km/s. The compression waves exhibited by this system are expected to have properties qualitatively similar to those of the higher density system to the extent that shocks with speeds greater than 12.5 km/s will be stable, single shocks and that shocks to lower densities are likely to have a ramp wave component due to the anomalous curvature of the isentrope. The leading edge of the ramp wave will propagate at 12.5 km/s.

Figure 5(b) shows the material density in an NEMD simulation when the piston is given a speed of 5.5 km/s. The resulting wave propagates at a steady speed of 13.4 km/s and appears to be a single, steady shock wave as predicted by

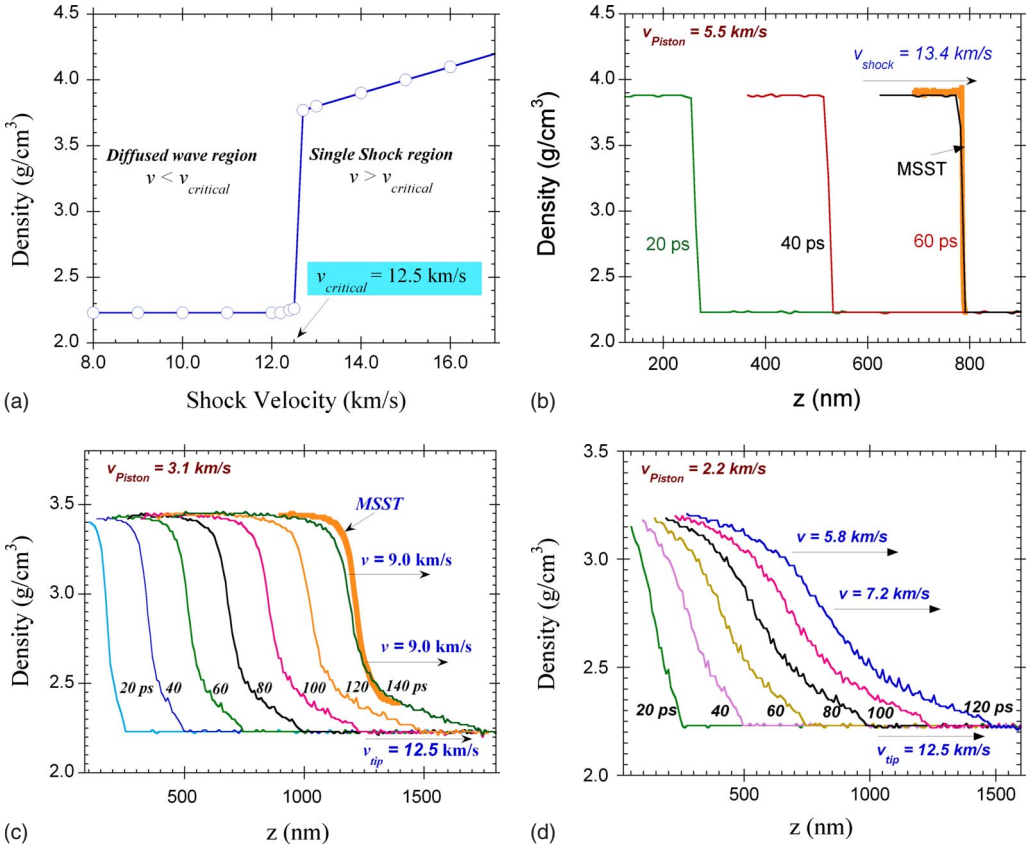

FIG. 5. (Color online) Results on less-dense a-carbon (ρ=2.23 g/cm^3). (a) MSST-computed final density (after 500 ps simulation time) as a function of shock velocity. There is a sharp discontinuity in density at $v_{\text{critical}} \sim 12.5$ km/s. (b) NEMD results for shock velocity of 13.4 km/s ($v > v_{\text{critical}}$) showing a sharp front, in agreement with MSST front (orange) at this velocity. (c) and (d) NEMD-computed wave propagation for the case $v < v_{\text{critical}}$ displaying a slanted front and a pronounced foot, whose tip travels at speed v_{critical}. An orange MSST simulation starting at the end of the unsteady foot is shown in (c). The higher density portion of (c) propagates at a steady 9 km/s while the analogous portion in (d) is unsteady. See text for details.

MSST. The density of an MSST simulation with shock speed chosen to be 13.4 km/s is overlaid in orange and reveals good agreement with the density and time scale of the NEMD shock.

Figure 5(c) shows the material density in an NEMD simulation when the piston is given a slower speed of 3.1 km/s. The resulting wave appears more spread out than in the high initial density cases considered and exhibits no sharp features. The top part of the wave, from density about 2.5 g/cm^3 and up, appears to propagate at a steady speed of 9.0 km/s suggesting it is likely a shock wave. The relatively slow rise of this wave suggests that the time scale is determined by the kinetics of chemical processes within the material. Purely elastic shock waves generally have much faster rise times on the order of optical phonon periods or on the order of 10 nm in space. The lower density part of the wave appears to have the ramp wave quality of spreading out with time. The leading edge of the wave propagates around 12.5 km/s. A naive view of this wave indicates that there are at least two different kinds of waves present.

Since MSST describes only steady shocks, it alone cannot simulate the wave in Fig. 5(c). However, MSST can be used to simulate the nearly steady, higher density portion. We have performed a MSST simulation starting around the density at the top of the unsteady foot, 2.39 g/cm^3, shown in orange in Fig. 5(c). We obtained the starting configuration for the MSST simulation by uniaxially straining the computational cell from the initial density 2.23 to 2.39 g/cm^3 over a period of 10 ps. This strain was performed adiabatically to mimic the conditions of the ramp compression process. The shock speed utilized for the MSST simulation was chosen by matching the final particle speed achieved to the 3.1 km/s piston speed of the NEMD simulation. The final particle speed achieved in the MSST simulation was 2.4 km/s which provides the 3.1 km/s material speed when combined with the 0.7 km/s speed of the 2.39 g/cm^3 material. The shock speed of this MSST simulation was found to be 7.8 m/s, yielding a 8.5 km/s propagation speed in the laboratory frame when combined with the 0.7 km/s speed of the 2.39 g/cm^3 material at the top of the unsteady portion. The 8.5 km/s speed should be compared with the 9.0 km/s observed propagation speed of the NEMD shock. Some level of discrepancy both in the propagation speed and wave profile in Fig. 5(c) are likely due to some unsteady character of the wave or appropriate choice of transition density from unsteady to steady portions of the wave.

Figure 5(d) is a simulation with a 2.2 km/s piston speed, slower than in Fig. 5(c). Unlike Fig. 5(c), the higher density

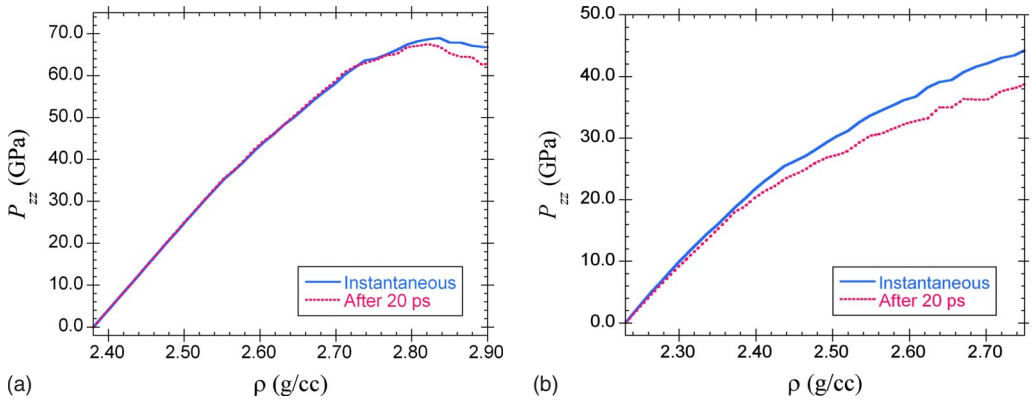

FIG. 6. (Color online) Instantaneous stress and stress after 20 ps in the direction of shock propagation (P_{zz}) as a function of density (ρ) for uniaxially strained: (a) dense a-carbon (starting ρ=2.38 g/cm^3) showing chemical changes above 2.8 g/cm^3; and (b) less-dense a-carbon (starting ρ=2.23 g/cm^3) showing chemical changes above 2.4 g/cm^3. These plots provide an approximate picture of the density regimes in which the dynamic compression waves are undergoing chemical changes.

portion of the wave appears to exhibit propagation speeds that vary with density, indicating the wave is unsteady. The lower density part appears to spread out with time.

Some insight into the nature of the various components of these waves can be obtained through calculation of the longitudinal pressure as a function of density shown in Fig. 6. The configuration at each density point in Fig. 6 was obtained by uniaxially straining a computational cell and scaling the atomic positions from the initial density configuration. Since amorphous materials can potentially exhibit chemical changes with even small density changes, these curves may exhibit a time dependence. The blue (solid) curves in Fig. 6 correspond to the stress exhibited instantaneously after the change in density. The red (dotted) curves are the stress exhibited after the system is allowed to evolve for 20 ps at 300 K with a constant T constraint. Constant energy (adiabatic) constraint simulations yield similar results. Stresses were calculated by averaging over 0.6 ps. The red (dotted) and blue (solid) curves do not overlap in regions where the material undergoes chemical changes on the 20 ps time scale, the rough time scale of the waves that we are studying in this work.

Figure 6(a) shows that on the 20 ps time scale, the lowest density to exhibit chemical changes is around 2.8 g/cm^3 for the higher initial density material. This indicates that the structure observed in Fig. 3(c) below 2.8 g/cm^3 density is can be attributed to the shape of the elastic equation of state (EOS) rather than time-dependent EOS properties involving chemical changes. For the lower initial density material, Fig. 6(b) shows that chemical changes occur at much lower densities of 2.4 g/cm^3 and possibly below. As in the higher density case, this indicates that the lower density parts of the waves in Figs. 5(c) and 5(d) are largely elastic despite the relatively slow rise.

The MSST calculations for both the high and low-density cases suggest that the material isentrope exhibits an anomalous region of negative curvature in $p_{zz}-\rho$ space around the initial density, i.e., $\frac{\partial^2 p_{zz}}{\partial \rho^2}|_S<0$, or $\frac{dc}{d\rho}<0$. This is most easily checked by considering the sound speeds calculated from the data in Fig. 6. Figure 7 shows the sound speeds calculated by taking the density derivative of the instantaneous p_{zz} vs ρ curve. Sound speeds calculated from the 20 ps curve are qualitatively similar.

Figure 7(a) for the denser material shows that the sound speed is roughly constant from the initial density ρ =2.38 g/cm^3 to around 2.45 g/cm^3 when it decreases with increasing ρ. This anomalous behavior suggests that a wave

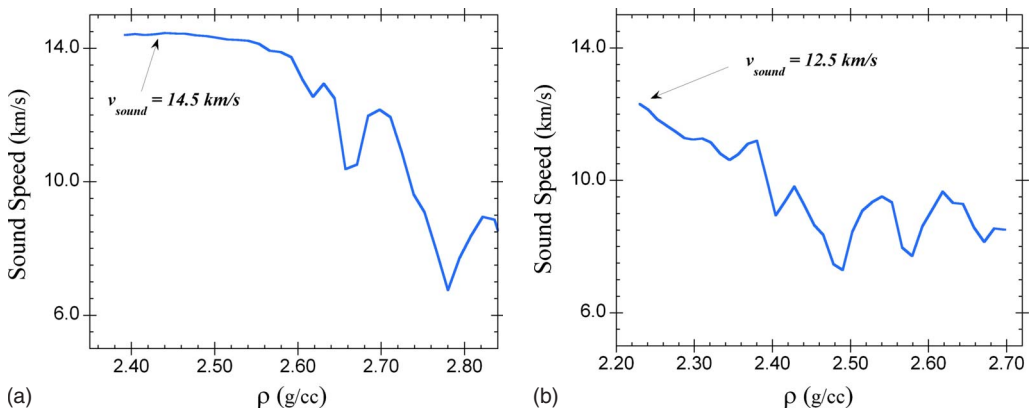

FIG. 7. (Color online) Longitudinal sound speed ($\sqrt{\frac{\partial P_{zz}}{\partial \rho}}$) as a function of density ρ for: (a) dense a-carbon (starting ρ=2.38 g/cm^3); and (b) less-dense a-carbon (starting ρ=2.23 g/cm^3). These curves exhibit anomalous behavior, decreasing with density over some regimes. This behavior leads to unsteady ramp waves when the material is dynamically compressed.

TABLE I. Some characteristics of types of planar waves that can be observed under dynamic compression, starting from an initial shock wave. Steady waves are those in which all parts of the wave propagate at the same speed.

	Steady (shock)	Unsteady (ramp)
Elastic	Fast rise time, on the order of optical phonon period.	Slower rise time, associated with $\frac{\partial^2 p_{zz}}{\partial V^2} < 0$ on the elastic isentrope. Will not form a shock.
Plastic or chemically reactive	Rise time slower than phonon oscillation period.	May form plastic shock at late times.

generated in this material will retain the temporal character of the drive at lower ρ followed by a more disperse ramp wave at higher densities. Such is the behavior exhibited by material in Fig. 3(c). The higher density feature in Fig. 3(c) that propagates at 11.6 km/s has a lower density around 2.8 g/cm^3. Figure 7(a) shows that this density is approximately the smallest density that can support a shock at that speed; i.e., sound speeds above this density are smaller than 11.6 km/s. The 14.8 km/s propagation speed of the wave in Fig. 3(b) is faster than the sound speeds in Fig. 7(a) indicating that this wave is a shock.

Figure 7(b) for the less-dense material shows that the sound speed decreases from the initial density $\rho = 2.23$ g/cm^3 to around 2.5 g/cm^3. This anomalous behavior suggests that a wave generated in this material will exhibit a ramp wave in this density range. Such is the behavior exhibited by material in Figs. 5(c) and 5(d). The feature at densities above 2.5 g/cm^3 propagating at 9.0 km/s in Fig. 5(c) is probably a shock since it is propagating faster than the sound speeds in this density regime. The nature of the unsteady feature at densities above 2.5 g/cm^3 in Fig. 5(d) is less clear. It may be an unsteady shock evolving into a steady shock on a time scale determined by the rate of chemical changes in the material. It could also maintain its unsteady character indefinitely or form a combination of shocks and unsteady waves.

IV. DISCUSSION

Four distinct kinds of waves are observable in the simulations of Figs. 3 and 5, summarized in Table I. In both cases, the lowest density features are characterized by elastic compression. The low-density features in Figs. 3(c), 5(c), and 5(d) are unsteady ramp waves associated with $\frac{\partial^2 p_{zz}}{\partial V^2} < 0$ on the elastic isentrope with the exception of the case of Fig. 3(c) where a fast rise can be observed at the leading edge of the wave. The ~nm length scale rise distance of this feature suggests it is a shock. The higher density features in Figs. 3 and 5 are associated with plastic deformation. The high density in Fig. 5(c) appears to be steady and therefore a shock, but the higher density feature in Fig. 5(d) is unsteady, i.e., different density portions of the wave propagate at different speeds. This wave may evolve into a steady shock if allowed to propagate for sufficient time.

Table I gives some distinguishing qualities of these four different types of waves which can be generated under rapid dynamic compression. Some of these qualities can be utilized to identify the type of wave from a hydrodynamic profile. For example, elastic shocks are the only waves that have rise times on the order of an optical phonon period.

This work is focused on the case where the initial wave launched into the material has a nearly instantaneous rise time. Waves generated by various experimental approaches can have rise times from 1 ps to nanoseconds and longer for laser platforms. Slower drives add some additional diversity in the types of wave behavior than can be observed. In particular, wave steepening processes can point to shock wave formation.

V. CONCLUSIONS

We have performed molecular-dynamics simulations of shocked amorphous carbon using the Tersoff potential and find that a variety of dynamic compression features appear for two different initial densities. These features include steady elastic shocks, steady chemically reactive shocks, unsteady elastic waves, and unsteady chemically reactive waves. We show how these features can be distinguished by analyzing time-dependent propagation speeds, time-dependent sound speeds, and comparison to MSST simulations. In addition to the direct simulations of dynamic compression, we employ the (MSST and find agreement with the thermodynamic states exhibited by the direct method. We show how the MSST can be extended to include explicit material viscosity and demonstrate on an amorphous Lennard-Jones system.

ACKNOWLEDGMENTS

This work was performed under the auspices of the U.S. Department of Energy by Lawrence Livermore National Laboratory under Contract No. DE-AC52-07NA27344.

[1] R. F. Smith, J. H. Eggert, A. Jankowski, P. M. Celliers, M. J. Edwards, Y. M. Gupta, J. R. Asay, and G. W. Collins, Phys. Rev. Lett. **98**, 065701 (2007).
[2] J.-P. Davis, J. Appl. Phys. **99**, 103512 (2006).
[3] D. K. Bradley, J. H. Eggert, R. F. Smith, S. T. Prisbrey, D. G. Hicks, D. G. Braun, J. Biener, A. V. Hamza, R. E. Rudd, and G. W. Collins, Phys. Rev. Lett. **102**, 075503 (2009).
[4] R. Fowles and R. F. Williams, J. Appl. Phys. **41**, 360 (1970).
[5] M. Cowperthwaite and R. F. Williams, J. Appl. Phys. **42**, 456 (1971).
[6] J. B. Aidun and Y. M. Gupta, J. Appl. Phys. **69**, 6998 (1991).
[7] L. M. Barker and R. E. Hollenbach, J. Appl. Phys. **41**, 4208 (1970).
[8] H. Bethe and E. Teller, Ballistics Research Lab Report No. BRL-X-117, 1942.
[9] C. Gazis and T. J. Ahrens, Earth Planet. Sci. Lett. **104**, 337 (1991).
[10] S. Brygoo, E. Henry, P. Loubeyre, J. Eggert, M. Koenig, B. Loupias, A. Benuzzi-Mounaix, and M. R. L. Gloahec, Nature Mater. **6**, 274 (2007).
[11] M. D. Knudson, M. P. Desjarlais, and D. H. Dolan, Science **322**, 1822 (2008).
[12] D. J. Erskine and W. J. Nellis, Nature (London) **349**, 317 (1991).
[13] S. V. Zybin, M. L. Elert, and C. T. White, Phys. Rev. B **66**, 220102(R) (2002).
[14] K. McLaughlin, I. I. Oleynik, S. V. Zybin, M. L. Elert, and C. T. White, in *Shock Compression of Condensed Matter Proceedings*, edited by M. Elert, M. D. Furnish, R. Chau, N. C. Holmes, and J. Nguyen (AIP, New York, 2007), p. 321.
[15] N. A. Romero and W. D. Mattson, Phys. Rev. B **76**, 214113 (2007).
[16] C. J. Mundy, A. Curioni, N. Goldman, I. F. W. Kuo, E. J. Reed, L. E. Fried, and M. Ianuzzi, J. Chem. Phys. **128**, 184701 (2008).
[17] A. Kubota, M.-J. Caturla, J. S. Stolken, and M. D. Feit, Opt. Express **8**, 611 (2001).
[18] F. Barmes, L. Soulard, and M. Mareschal, Phys. Rev. B **73**, 224108 (2006).
[19] S.-N. Luo, L.-B. Han, Y. Xie, Q. An, L. Zheng, and K. Xia, J. Appl. Phys. **103**, 093530 (2008).
[20] J. Tersoff, Phys. Rev. Lett. **61**, 2879 (1988).
[21] E. J. Reed, L. E. Fried, and J. D. Joannopoulos, Phys. Rev. Lett. **90**, 235503 (2003).
[22] E. J. Reed, L. E. Fried, M. R. Manaa, and J. D. Joannopoulos, in *Chemistry at Extreme Conditions*, edited by M. R. Manaa (Elsevier, New York, 2005), pp. 297–326.
[23] M. R. Manaa, E. J. Reed, L. E. Fried, and N. Goldman, J. Am. Chem. Soc. **131**, 5483 (2009).
[24] N. Goldman, E. J. Reed, I.-F. W. Kuo, L. E. Fried, C. J. Mundy, and A. Curioni, J. Chem. Phys. **130**, 124517 (2009).
[25] E. J. Reed, M. R. Manaa, L. E. Fried, K. R. Glaesemann, and J. D. Joannopoulos, Nat. Phys. **4**, 72 (2008).
[26] E. J. Reed, L. E. Fried, W. D. Henshaw, and C. M. Tarver, Phys. Rev. E **74**, 056706 (2006).
[27] H. C. Andersen, J. Chem. Phys. **72**, 2384 (1980).
[28] L. Soulard, *Shock Compression of Condensed Matter 1999* (American Institute of Physics, New York, 2000), p. 185.
[29] J. B. Maillet, M. Mareschal, L. Soulard, R. Ravelo, P. S. Lomdahl, T. C. Germann, and B. L. Holian, Phys. Rev. E **63**, 016121 (2000).
[30] R. Ravelo, B. L. Holian, T. C. Germann, and P. S. Lomdahl, Phys. Rev. B **70**, 014103 (2004).
[31] A. V. Bolesta, L. Zheng, D. L. Thompson, and T. D. Sewell, Phys. Rev. B **76**, 224108 (2007).